International Journal of Mineral Processing 160 (2017) 47–57

Contents lists available at ScienceDirect

International Journal of Mineral Processing

journal homepage: www.elsevier.com/locate/ijminpro

Classification of rock lithology by laser range 3D and color images

Francisco J. Galdames*, Claudio A. Perez, Pablo A. Estévez, Martin Adams

Image Processing Laboratory, Department of Electrical Engineering; and Advanced Mining Technology Center (AMTC). Universidad de Chile, Av. Tupper 2007, Santiago, Chile

ARTICLE INFO

Article history:
Received 24 June 2016
Received in revised form 28 November 2016
Accepted 17 January 2017
Available online 19 January 2017

Keywords:
Rock classification
Laser range 3D features
Gabor features
LBP features
Range imaging

ABSTRACT

The determination of hardness and approximate mineral composition of rocks and classifying these lithologies aids in controlling various processes in the plant, such as reducing the grinding process, which accounts for about 50% of its energy consumption. In this paper, a new method for rock lithological classification is presented, based on color as well as 3D laser based features. The method uses color and laser range images, acquired from rocks on a conveyor belt, to compute Gabor and LBP (Local Binary Pattern) features. Various Gabor and LBP features are tested, including rotation invariant features. The images are tessellated into sub-images in which the features are computed. The classification is performed in two stages. In the first stage, the sub-images are classified by using a support-vector machine (SVM) classifier. In the second stage, the classification is improved by a voting process among all the sub-images of each rock. The method was tested on a database with five different rock lithologies taken from a copper mine which has been used in previous studies, allowing comparison with our new results. The results show that the classification performance was improved significantly by adding the 3D laser texture features, and using a combination of rotation invariant Gabor and LBP features, achieving a classification accuracy of 99.24% on the database. Using the CMIM (Conditional Mutual Information Maximization) feature selection method showed that only 10% of the total extracted features are required to achieve the maximum correct classification rate and that using the 3D laser features, (for the first time in our rock classification method to the best of our knowledge) is important for maintaining high classification performance.

1. Introduction

Rock type classification is of great importance in many stages of mine operations. Possible applications range from mine planning to the control of processes, such as grinding (Casali et al., 2001; Chatterjee et al., 2010b) which consumes about 50% of the energy used in a mining plant. For example, the energy employed in the mill operation could be optimized if the actual rock types and hardness could be determined, saving significant resources and reducing CO_2 production. Rock type could also be used to control the feeding and speed of the mill, minimizing energy consumption and optimizing the extraction process (Guyot et al., 2004; Tessier et al., 2007). Another possible application is ore sorting. Usually the classification and characterization of rocks is carried out visually by geologists and mineralogists, or by laboratory tests (Chatterjee et al., 2010b). Nevertheless, manual classification is time consuming, since it is sometimes necessary to stop the processing of the material for classification and impossible to apply at all during certain steps of the grinding process. Moreover, manual classification is only an approximation, because it is usually carried out using coarse sampling. Consequently, automatic rock classification would be beneficial, making it possible to address the previously mentioned applications and to provide a constant flow of information for controlling various tasks (Guyot et al., 2004). In the past, most studies have focused on the development of on-line methods to estimate rock size, with the objective of reducing power consumption and avoiding mill overload (Tessier et al., 2007). The first methods for estimating the size and shape of the rocks were based on 2D image analyses. Nevertheless, 2D methods have some restrictions (Potts and Ouchterlony, 2005; Thurley, 2009): such as the difficulty of identifying boundaries when rocks are of the same type and overlap each other. Such partially occluded rocks are often classified as smaller in size than they really are (Thurley, 2002).

One of the first methods to measure the size of rocks, using computer vision techniques in 2D images, was proposed by Carlsson and Nyberg (1983). In Oestreich et al. (1995), a system based on color images was presented for estimating the composition of rocks. This method used the angle between color vectors to estimate the composition of a mix of two minerals, chalcopyrite and molybdenite. In Perez et al. (1999), a method based on neural networks for classifying 7 different rock lithologies using color images was introduced.

* Corresponding author.
E-mail addresses: fgaldame@ing.uchile.cl (F.J. Galdames), clperez@ing.uchile.cl (C.A. Perez), pestevez@ing.uchile.cl (P.A. Estévez), martin@ing.uchile.cl (M. Adams).

http://dx.doi.org/10.1016/j.minpro.2017.01.008
0301-7516/

Other methods have been developed since then, such as the one presented in Casali et al. (2001), in which features were computed from 2D images. The features were optimized by genetic algorithms and used to classify the ore by a neural network. The energy required for the grinding process was also estimated. In Salinas et al. (2005), the size distribution of the rocks was estimated using filters, morphological operators, and the watershed transform method.

An industrial rock classification system that combines local texture information and co-occurrence likelihoods was introduced in Paclík et al. (2005). In Lepistö et al. (2005), a rock classification method which uses Gabor filters applied in different color spaces was introduced. A case study of classification of ferruginous manganese ore using histogram analysis in the RGB space, combined with textural analysis based on a co-occurrence matrix of gray levels and edge detection, was presented in Singh and Rao (2006).

In Wang (2006) the size of the rocks was approximated by the best-fit rectangle. A method was presented in Al-Thyabat et al. (2007), in which images of rocks on a conveyor belt were segmented semi-manually, and then the performances of different measures for estimating the size distribution of the rocks were evaluated. In Tessier et al. (2007) an automatic system mounted in a pilot plant for the estimation of rock mixture composition was presented. The classification method used a support vector machine (SVM) to classify 5 different minerals, and principal components analysis (PCA) and wavelet texture analysis (WTA) to extract color and textural features, respectively.

A method based on neural networks combined with PCA and frequency measures to classify 26 rock types was introduced in Kachanubal and Udomhunsakul (2008). In Murtagh and Starck (2008), a method using wavelets and curvelet moments to classify images of aggregates was presented. A classification method for rock textures based on a hierarchical neuro-fuzzy model was introduced in Gonçalves et al. (2009). In Al-Batah et al. (2009) neural networks were used with features extracted from 2D images to classify aggregates for concrete. In Koh et al. (2009), illumination from different angles was used to improve the segmentation of wooden spheres and pebbles in order to estimate size distribution.

A method that uses genetic algorithms, *k*-means clustering and neural networks to predict the ore grade in samples extracted from a drill-hole in a lead-zinc deposit was presented in Chatterjee et al. (2010a,b). A method to identify the texture of different basalts in RGB or grayscale images using a neural network was introduced in Singh et al. (2010). In Fernández et al. (2011) the performances of different types of Local Binary Patterns (LBP), Coordinated Clusters Representation (CCR) and ILBP (Improved Local Binary Patterns) were measured for the classification of granite tiles under rotations, concluding that the ILBPs were the best features. A system for aggregate classification was presented in Isa et al. (2011). The classification method extracts the Hu and Zernike moments from the rock segmentation, and the classification is performed by a neural network. A rock classification method that uses multi-way PCA to extract color features and Wavelet Texture Analysis (WTA) to compute texture features was presented in Perez et al. (2011). The method selects a subset of features using mutual information, and uses an SVM to perform the classification. The classification is improved by a voting process among the classified sub-images of each rock. The same voting method was used in Perez et al. (2015), using multi-scale Gabor features. In Bianconi et al. (2012) a classification system for granite tiles was presented. Different features were tested, and the best performance was obtained with co-occurrence matrices. A method to classify limestone rock-types by using color image histogram-based features and probabilistic neural network (PNN) was introduced in Patel and Chatterjee (2016).

Rock classification performance was improved with methods using shape and size information in laser range 3D images. The 3D information is not affected by color or illumination variations. Moreover, using 3D information, it is easier to detect the rocks near the surface without occlusions, to classify shape, and to improve segmentation. A method for segmenting aggregates on a conveyor belt using a laser triangulation scanner was introduced in Kim et al. (2003). The method used the Canny edge detector and the watershed transform. However, the rocks were isolated on the conveyor belt without occlusions among them in this study.

In Lee et al. (2005) a method for computing the angularity of rocks using 3D information acquired by laser triangulation was presented. The method used mathematical morphology techniques to simulate the natural wear process that makes rock particles become rounded. In Thurley and Ng (2005), a method to segment the surface of rock piles using 3D information was presented. Irregularly spaced 3D coordinate surface data was processed using morphology operators and image segmentation algorithms. The same method was used in Thurley and Ng (2008), but extended to detecting partially occluded rocks on the surface of rock piles. In Thurley (2009), laser triangulation was used to measure rock size inside underground LHD (Load-Haul-Dump) unit buckets. The method takes overlapping rocks into account, and identifies areas of fine material below the resolution of the 3D sensor. In Thurley and Andersson (2008), a method for measuring the size of iron ore green pellets on a conveyor belt by using a laser triangulation acquisition system was presented. The method identified non-overlapped pellets, and used mathematical morphology techniques, and the watershed transform. The same method was used in Thurley (2011) to measure the size distributions of limestone particles on a conveyor belt.

Textures have specific orientations for some rock lithologies as has been reported in previous research for classifying types of granites (Bianconi et al., 2012; Fernández et al., 2011), but they have not been included in general ore classification. Accordingly, features that include rotation invariance are considered in this work. Some methods achieve rotation invariance by performing a transformation of the features into another space, for example, by using the Discrete Fourier Transform (DFT). The shift invariance property of the DFT is used in Riaz et al. (2013) to build rotation and scale invariant Gabor features, and the DFT of histograms of LBP is used in Zhao et al. (2012) to achieve rotation invariance. Other methods perform a rearrangement of feature vectors, such as in Hegenbart and Uhl (2015), where the rotation invariance of LBP is achieved by explicit alignment of features at the extraction level using a robust estimate of global orientation. In Arivazhagan et al. (2006), the rotation invariance of Gabor features is achieved by a circular shift of the features according to the orientation with the highest total energy. Other methods compute features or statistics across the features obtained at different angles; for example, in Han and Ma (2007), the rotation invariance of Gabor features is achieved by the summation of the Gabor filters along the different angles on the same scale. Some methods use features that take rotation invariance into account implicitly, such as the rotation invariant LBP (Ojala et al., 2002). All the strategies to achieve rotation invariance mentioned above are taken into account in this work. The features used are explained in Section 2.3. In previous cited papers above the problem of lithology classification is addressed using 2D images. In the literature, 3D range images have been used to address only the problem of size estimation.

In this work, we introduce 3D laser range images to improve lithological classification. Our proposed method extracts color features as well as 3D laser range features for classifying the rock type. Our hypothesis is that classification performance can be improved by combining 3D laser range and color features. Invariant features have shown to be very relevant in image processing, see for example Lecun et al. (1998), Perez et al. (2010, 2007), Zhang and Tan (2002). Additionally, our method uses both color and the 3D data for rock segmentation. First, the images are tessellated into sub-images which are classified by using color and 3D texture features. Then, the rocks of each image are segmented to improve classification by

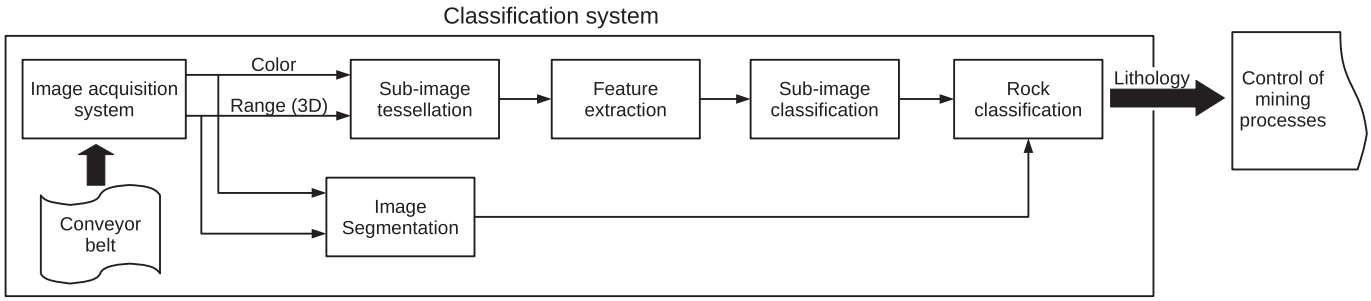

Fig. 1. Block diagram of the proposed lithological classification method.

a voting process among the sub-images of each rock. The method is validated on a database with 5 different rock lithologies.

2. Methods and materials

The lithological classification method proposed in this paper is based on color and laser range (3D) images. Fig. 1 shows a block diagram of the proposed method. The images are tessellated into sub-images where features are computed. A SVM is used to classify the lithology of each sub-image by using the extracted features. With the purpose of improving rock classification, the rocks are segmented, and a voting process is performed among the sub-images of each rock.

2.1. 3D range image and color image acquisition systems

A SICK ColorRange Ranger-E55444 camera[1] was mounted perpendicular to a conveyor belt for data acquisition. This camera can acquire 3D range and high-definition color images. The camera is equipped with a CMOS sensor which is used as a line-scan, acquiring the images line by line as objects move. The CMOS sensor has 15 high resolution lines with 3072 columns. Three of these lines are used to acquire the red, green, and blue channels of the color images using LED illumination. Another section of the CMOS sensor has an infrared-pass filter. This section is composed of 411 lines with 1536 columns, and is used to acquire the range image by infrared (IR) laser triangulation. An IR laser was mounted at 45° in relation to the conveyor belt. The laser projects a line that is deformed as the rocks move on the conveyor belt, and this deformation is detected along the columns of the CMOS sensor with the infrared-pass filter. The 3D surface of the rocks is computed by using the laser line deformation and a previous calibration. Fig. 2 shows the complete acquisition system for the laser range and color images.

As explained above, the acquired color and range images are composed of 3072 and 1536 columns, respectively. The images were transformed, obtaining images of 3017 columns with isotropic pixels of approximately 0.12 × 0.12 mm. The resolution of the range image is approximately 0.0234 mm. on the z axis. Fig. 3 (a) and (b) show a color and a range image, respectively. Fig. 3 (c) shows the range image superimposed on the registered color image.

2.2. Rock segmentation in range and color images

After registering the color and range images, rocks are segmented to be able to classify each rock type. Range images are segmented first because it is simpler to identify each rock in the range images.

Range images contain noise produced by reflections of ambient light from the rock surfaces. Morphological closing and opening is performed with a square structural element of 3 × 3 pixels to reduce the noise. Because laser triangulation is performed in only one direction, the range images have some areas without information corresponding to occlusions of the laser by the rocks. The rock boundaries are identified using the edges of the occluded areas and the range information (Thurley, 2011). The occlusion areas are binarized and those with areas of less than 40 mm^2 of area are ignored. The remaining areas are dilated by a structural element of 3 × 3 and the original binary image is subtracted to find the edges. Then, morphological closing with the same structural element is applied. Next, the range information is used to detect rock edges. The difference between the dilation and erosion of the range image by a 3 × 3 structural element is used to compute its gradient. Gradients of more than 5 mm of depth and 4 mm of length are binarized and kept as edges. These new edges are combined with the edges computed from the occlusion areas, and the distance transformation is computed in the obtained image. Then, the morphological h-maxima operation is used to detect the local maxima of less than 4 mm. The maxima which do not occur in occlusion areas are binarized and filtered using the seed growing algorithm (Thurley and Andersson, 2008; Thurley and Ng, 2005). Next, the watershed algorithm (Beucher and Lantuéjoul, 1979; Bieniek and Moga, 2000) is used to obtain the segmentation of the range image. The binarized maxima are used as seeds of the watershed transformation applied to the gradient of the range image. After segmentation, the known range level

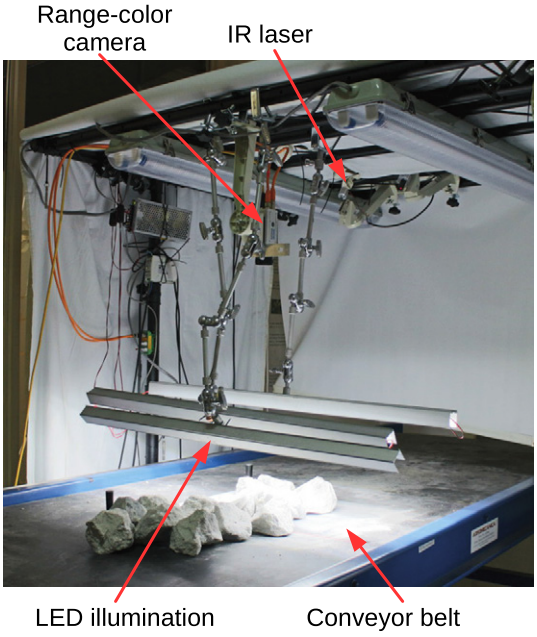

Fig. 2. Acquisition system for 3D laser range and color images.

[1] http://www.sick.com/group/EN/home/products/product_portfolio/vision/Pages/high-end_cameras.aspx

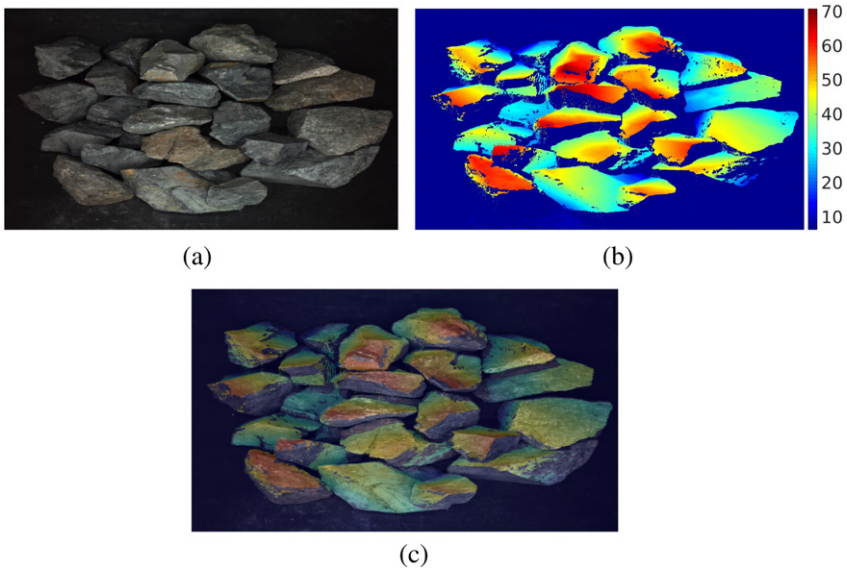

Fig. 3. Registration of range and color images. (a) Color image. (b) Range image where the color represents the height in mm. (c) Range image registered and superimposed on the color image.

of the conveyor belt in the range image is used to detect the areas of segmentation that correspond to the background. Finally, the borders between each segmented object and its neighbors are analyzed to detect objects that correspond to the same rock. The objects that share an edge of less than 5 mm of depth and 20 mm of length are combined as part of the same rock. Fig. 4 (a) shows an example of the range image segmentation technique.

The color image is segmented after the range image. First, the color image is transformed into grayscale, and a bilateral filter (Chaudhury, 2013) is used to smooth the surface of the rocks without affecting their boundaries. The watershed algorithm (Beucher and Lantuéjoul, 1979; Bieniek and Moga, 2000) is applied to the gradient of this gray image for segmentation. Because there are both rocks and background (conveyor belt) in our images, we need to compute rock and background seeds to be used in the watershed algorithm. To find the rock seeds, the segmentation of the range image is binarized and eroded by a 30 × 30 structural element. Seeds for the background are obtained using the range and the gray level image, as follows: The gray level value corresponding to the peak of the gray image histogram in a test area of the conveyor belt is considered to be the background gray level threshold. The gray level image is binarized using this background, considering the pixels below the threshold as background seeds. The pixels with a height lower than 5 mm over the known level of the conveyor belt in the range image are also considered to be background seeds. If there are intersections between the background and rock seeds, these intersections are removed from the background seeds. Moreover, in order to be sure if any background seed intersects a rock, its size is reduced as follows: The distance transform of the background seed image complement is computed, and only the seed pixels that have a distance less than the mean of the distance transform in each seed are kept. Finally, the rocks and background seeds are used in the watershed algorithm. Fig. 4 (b) shows the segmentation of a color image.

2.3. Feature extraction in range and color images

Features are extracted from the range and color images which are tessellated into sub-images of 60 × 60 pixels, in a similar way to that proposed by Tessier et al. (2007). The pixels of each sub-image may belong to different rocks placed side by side, or in different heights if one occludes a portion of another. Also, some pixels of one sub-image may belong to the background (conveyor belt). The problem of having background or more than one rock in one sub-image is addressed in Section 2.4.

All extracted features are computed within the sub-image. These features are based on Gabor filters, Local Binary Patterns (LBP), and chromatic features. Gabor filters and LBPs are complementary features, because the Gabor filter can extract global features, whereas LBP captures the local structure of the texture (Liao et al., 2009; Liu et al., 2014). The texture features based on Gabor filters and LBP are computed in the range and color images, and are then concatenated to build a feature vector. The color image is transformed into the HSV space, and then the texture features are computed in each of the three channels. In order to investigate the effect of separating texture

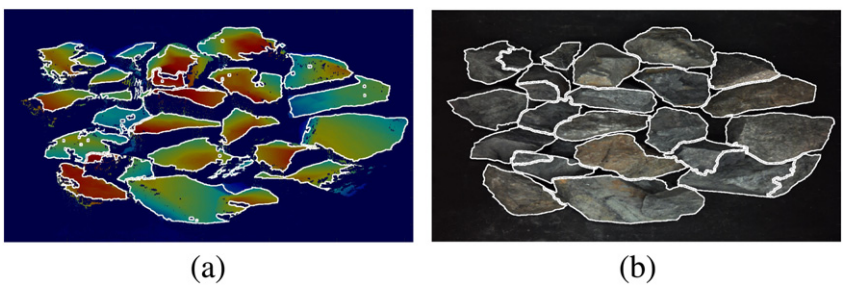

Fig. 4. Registration and segmentation of range and color images. (a) Segmentation of the range image. (b) Segmentation of the color image.

and color information, the images were also classified using texture features (Gabor filters, LBP) computed in grayscale. In this way, the classification is performed by using texture information computed in grayscale, and chromatic features computed in the HSV space which are described in Section 2.3.3.

2.3.1. Gabor features for feature extraction from rocks

Gabor filters are frequency filters, localized in space, and with a particular orientation. Gabor features are computed using 5 scales defined by $0 \leq \nu \leq 4$, and 8 orientations defined by $0 \leq \mu \leq 7$. The Gabor filters are defined by:

$$\Psi_{\nu,\mu}(x,y) = \exp\left(-\frac{\left|\vec{k}\right|^2\left|\vec{r}\right|^2}{2\sigma^2}\right)\left(\exp\left(i\vec{k}\cdot\vec{r}\right) - \exp\left(-\sigma^2/2\right)\right), \quad (1)$$

where vectors $\vec{r} = \begin{bmatrix} x \\ y \end{bmatrix}$ and $\vec{k} = \frac{\pi}{2f^{\nu}}\begin{bmatrix} \cos(\mu\pi/8) \\ \sin(\mu\pi/8) \end{bmatrix}$, and constants $f = \sqrt{2}$ and $\sigma = \pi$. The spatial scale is equivalent to $\lambda \in \left\{4, 4\sqrt{2}, 8, 8\sqrt{2}, 16\right\}$ in pixels. In order to extract Gabor features, a convolution between the Gabor filters and the sub-images is performed, i.e.,

$$G_{\mu,\nu,i}(x,y) = \Psi_{\nu,\mu} * I_i, \quad (2)$$

where I_i is the sub-image i of image I. Since Gabor filters are complex, the values of $G_{\mu,\nu,i}(x,y)$ are complex numbers, and can be represented by their magnitude $M_{\mu,\nu,i}(x,y) = |G_{\mu,\nu,i}|$ and phase $\Phi_{\mu,\nu,i}(x,y) = \arg(G_{\mu,\nu,i})$. The magnitude $M_{\mu,\nu,i}$ gives information about the frequencies presented, and the gradient of the phase $\mathcal{G}_{\mu,\nu,i}(x,y) = \nabla(\Phi_{\mu,\nu,i})$ gives information about how these frequencies change. Accordingly, the first Gabor features computed in each sub-image are the mean and the standard deviation of the magnitude, $\overline{M_{\mu,\nu,i}}$, std$(M_{\mu,\nu,i})$, respectively; and the mean and the standard deviation gradient of the phase $\overline{\mathcal{G}_{\mu,\nu,i}}$, std$(\mathcal{G}_{\mu,\nu,i})$, respectively. Different Gabor features are computed using these Gabor basic features, some of which include rotation invariance: G_{stat}, G_{rea} and G_{DFT}. The computed Gabor features for classification are the following:

G_M: Using the features $\overline{M_{\mu,\nu,i}}$ and std$(M_{\mu,\nu,i})$. These features consider scale and orientation; however, they include neither rotation invariance nor the phase of the Gabor filters.
G_{MP}: Using the features $\overline{M_{\mu,\nu,i}}$, std$(M_{\mu,\nu,i})$, $\overline{\mathcal{G}_{\mu,\nu,i}}$ and std$(\mathcal{G}_{\mu,\nu,i})$. These features do not consider rotation invariance.
G_{stat}: The features G_{stat} consider rotation invariance by computing simple statistical values across the angles. The mean and standard deviation of the features $\overline{M_{\mu,\nu,i}}$, std$(M_{\mu,\nu,i})$, $\overline{\mathcal{G}_{\mu,\nu,i}}$ and std$(\mathcal{G}_{\mu,\nu,i})$, are computed across the angles of each scale, and are used as features. In this way, 8 features are obtained in each spatial scale.
G_{rea}: The features G_{rea} are the same as those used in G_{MP}, however G_{rea} considers rotation invariance. The rotation invariance is achieved by rearranging the features according to an angle. The mean of $\overline{M_{\mu,\nu,i}}$ is computed across the scales in every orientation, and the orientation $\mu^{\max}$ with maximum value is considered as the reference:

$$\mu_i^{\max} = \arg\max_{\mu} \sum_{i=0}^{4} \overline{M_{\mu,\nu,i}}. \quad (3)$$

Then, the features $\overline{M_{\mu,\nu,i}}$, std$(M_{\mu,\nu,i})$, $\overline{\mathcal{G}_{\mu,\nu,i}}$ and std$(\mathcal{G}_{\mu,\nu,i})$ are rearranged according to $\mu_i^{\max}$ and used in the classification process.
G_{DFT}: Although the features G_{DFT} use the same features as G_{MP}, nevertheless a rotation invariance is achieved by using the shift invariance property of the DFT. The DFTs of the features $\overline{M_{\mu,\nu,i}}$, std$(M_{\mu,\nu,i})$, $\overline{\mathcal{G}_{\mu,\nu,i}}$ and std$(\mathcal{G}_{\mu,\nu,i})$ are computed across the orientations, in every scale. Then these DFTs are used as features for the classifying process.

2.3.2. Local binary patterns for feature extraction from rocks

The LBP features use binary comparisons between pixels by sampling within a neighborhood around each pixel where the code is computed to characterize texture. The gray level of a pixel x_c is compared with the gray levels of p neighbors evenly distributed in a circle of radius r (Ojala et al., 2002):

$$\mathrm{LBP}_{r,p} = \sum_{n=0}^{p-1} s\left(x_{r,p,n} - x_c\right) 2^n, \; s(x) = \begin{cases} 1, & x \geqslant 0 \\ 0, & x < 0 \end{cases}. \quad (4)$$

The LBP is computed at each pixel in the image, and the texture is described by the histogram vector of these LBPs. Given p neighbors, the maximum number of different LBPs is 2^p. In order to perform a multi-resolution analysis, LBPs with different radius r are computed, and the resulting histograms are concatenated to build the feature vector. The number of neighbors used in this work was $p = 8$, and the scales $r = \{1, 3, 5, 7, 9\}$. Two types of LBP features were used for comparison, which are described as follows:

LBP^{riu2}: The Rotation Invariant Uniform patterns, LBP^{riu}, were proposed in Ojala et al. (2002). These LBPs use a uniformity measure U, which corresponds to the number of spatial transitions (0/1) in the binary pattern ($s(x)$). The number of transitions proposed in Ojala et al. (2002) is at most 2. The LBP^{riu2} also considers that all the rotated versions of the same binary pattern correspond to the same feature. The result is a rotation invariant feature described by:

$$\mathrm{LBP}_{r,p}^{riu2} = \begin{cases} \sum_{n=0}^{p-1} s\left(x_{r,p,n} - x_c\right) & \text{if } U(\mathrm{LBP}_{r,p}) \leqslant 2 \\ p+1 & \text{otherwise,} \end{cases} \quad (5)$$

where

$$U(\mathrm{LBP}_{r,p}) = \sum_{n=1}^{p-1} \left|s(x_{r,p,n} - x_c) - s(x_{r,p,n+1} - x_c)\right|. \quad (6)$$

The histogram vector of the LBP^{riu2} computed in the image is used as the feature vector.
BRINT_CS_CM: The BRINT (Binary Rotation Invariant and Noise Tolerant) LBP was proposed in Liu et al. (2014). It is invariant under rotation, and includes local thresholds, and an average in the sampling of pixels in the neighborhood to achieve more robustness. The BRINT_CS_CM is computed by using three types of LBPs: BRINT_S (BRINT_Sign), BRINT_M (BRINT_Magnitude), and BRINT_C (BRINT_Center) which will be explained in the following:

First, the neighbors of x_c are grouped in p arcs of q points, and an average is taken from each group:

$$y_{r,p,i} = \frac{1}{q}\sum_{k=0}^{q-1} x_{r,pq,(qi+k)}, \; i = 0, \ldots, p-1. \quad (7)$$

Then, a LBP called BNT_S (Binary Noise Tolerant Sign) can be computed by comparing the means $y_{r,p,i}$ with the central pixel x_c:

$$\mathrm{BNT\_S}_{r,p} = \sum_{n=0}^{p-1} s(y_{r,p,n} - x_c) 2^n. \quad (8)$$

Rotation invariance is introduced to compute the BRINT_S. Equal versions of binary representations under rotations are grouped by assigning code numbers to the resulting groups in the same way as used in the rotation invariant version of the LBP (Pietikäinen et al., 2000):

$$\mathrm{BRINT\_S}_{r,p} = \min\left(\mathrm{ROR}(\mathrm{BNT\_S}_{r,p}, i) | i = 0, \ldots, p-1\right), \quad (9)$$

where $\mathrm{ROR}(x, i)$ performs a circular i-step bit-wise right shift on x, i times.

The BRINT_M is based on the complementary LBP, CLBP_M (CLBP-Magnitude), proposed in Guo et al. (2010). The BRINT_M performs comparisons between x_c and a local threshold to generate the binary code. First, the absolute value of the local differences between x_c and its neighbors are computed:

$$\Delta_{r,pq,i} = \left|x_{r,pq,i} - x_c\right|, \; i = 0, \ldots, p(q-1). \quad (10)$$

Then, the means, $z_{r,p,i}$, of the $\Delta_{r,pq,i}$ are computed in each of the p arcs, as in Eq. (7):

$$z_{r,p,i} = \frac{1}{q}\sum_{k=0}^{q-1} \Delta_{r,pq,(qi+k)}, \; i = 0, \ldots, p-1. \quad (11)$$

The $z_{r,p,i}$ are used to compute the BNT_M (BNT_Magnitude) binary pattern:

$$\mathrm{BNT\_M}_{r,p} = \sum_{n=0}^{p-1} s(z_{r,p,n} - \mu_{r,p})2^n, \quad (12)$$

where $\mu_{r,p}$ is a local threshold computed as:

$$\mu_{r,p} = \frac{1}{p}\sum_{n=0}^{p-1} z_{r,p,n}. \quad (13)$$

The BRINT_M local binary pattern is defined by using the BNT_M as:

$$\mathrm{BRINT\_M}_{r,p} = \min\left(\mathrm{ROR}(\mathrm{BNT\_M}_{r,p}, i) | i = 0, \ldots, p-1\right). \quad (14)$$

The last LBP included in the BRINT_CS_CM is the BRINT_C which represents the center pixel in one of two bins:

$$\mathrm{BRINT\_C}_r = s(x_c - \mu_{l,r}), \quad (15)$$

where $\mu_{l,r}$ is a threshold defined as the mean of the whole image excluding boundary pixels:

$$\mu_{l,r} = \frac{1}{(M-2r)(N-2r)}\sum_{i=r+1}^{M-r}\sum_{j=r+1}^{N-r} x(i,j). \quad (16)$$

Finally, the $\mathrm{BRINT\_CS\_CM}_{r,p}$ descriptor is the joint histogram $\mathrm{BRINT\_C} * \mathrm{BRINT\_S}_{r,p}$ concatenated with $\mathrm{BRINT\_C} * \mathrm{BRINT\_M}_{r,p}$. As recommended in Liu et al. (2014), the value of q was 1 for $r = 1$, and $q = 3$ in the other scales.

2.3.3. Chromatic features for rock classification

Two chromatic features are extracted, besides the texture information in gray scale. The image is transformed into the HSV color space, and then the mean and standard deviation of the H and S channels are used as chromatic features. These chromatic features are used together with the texture features (Gabor filters, LBPs) computed on the image in gray levels.

2.4. Classification

Lithological classification is performed in two stages: classification by sub-image, and classification by rock, which are described as follows:

2.4.1. Classification by sub-image

The computed features are concatenated, obtaining a feature vector in each sub-image. For example, 80 features are obtained if the G_M features are computed with 8 orientations and 5 scales; and 50 features are obtained if the LBP^{riu2} features are computed using 8 neighbors and 5 scales. Therefore, a feature vector of length 520 is created for each sub-image, if the G_M and LBP^{riu2} features are used in color (3 channels) and range (1 channel) images.

Since the aim of our work is to propose a new and improved method for lithological classification of rock using new features, a state-of-the-art classification method must be used to evaluate the performance obtained by using the different features. The Random Forest and the SVM were the classifiers with best performance in Fernández-Delgado et al. (2014), where 179 classifiers arising from 17 families were evaluated. Also, the SVM has become a very popular classification method because of excellent results in many different fields. For these reasons, an SVM is used in this work to classify each sub-image using its feature vector. The publicly available LibSVM (Chang and Lin, 2011) implementation of SVMs was used. The C-SVC (Support Vector Classification) SVM formulation was used (Cortes and Vapnik, 1995), which maps input vectors using a non-linear transformation to a high-dimensional space where linear decision hyperplanes are constructed for class separation. Radial basis functions ($K(u, v) = \exp(-\gamma * |u - v|^2)$) were used as kernel functions to map the input vector. The optimal values for the regularization parameter C of the SVM (defined in Chang and Lin, 2011), and for the parameter γ of the radial basis functions, are searched in a subset of the data. As suggested in Chang and Lin (2011), the optimal values for parameters C and γ are searched using cross validation in a grid of parameters with logarithmic scale. In order to measure the performance of the method, the dataset is divided into subsets, and a cross validation is carried out using one subset as validation set and the other subsets as training set. The classifier is trained with the training set, and then is tested on the validation set using the sub-images as inputs. Since the rocks do not cover the whole image, the conveyor belt is visible in some sub-images. Only sub-images with more than 90% of rock, according to the color image segmentation method, are processed using the SVM. The others are discarded because most of them contain mostly background. Also, the pixels of one sub-image may belong to different rocks. This may produce a sub-image misclassification; nevertheless, these misclassifications are corrected in the classification by rock presented in Section 2.4.2.

2.4.2. Classification by rock

As described in Perez et al. (2011, 2015), the classification obtained by using the feature vectors from the sub-images can be improved by performing a voting process with all the sub-images that belong to a single rock. The sub-images that compose each rock are identified by using the color image segmentation method as described in Section 2.2. Sub-images with more than 50% of background in the segmentation stage are considered to be background and are not classified. Each sub-image that is not considered to be background is assigned to the rock with the largest area in it. Then, the most common lithology in the classified sub-images of each rock is identified. If the percentage of sub-images with this lithology in the rock is over a confidence threshold, all the sub-images within the rock are assigned to this lithology. This process corrects some

misclassified sub-images, improving the performance of the overall classification.

3. Database and experiments

A database was built using ore samples from a copper mine in Chile (Perez et al., 2015). The ore samples are composed of rocks that can be grouped into five different lithologies: Andesite (AN), Dacitic Diatreme (DD), Rhyolitic Diatreme (RD), Porphyritic Dykes (PD), and Other Breccias (OB). Sets of 40 range and color images were acquired for these five types of lithologies using a conveyor belt in the laboratory as shown in Fig. 2. Different images of the same samples were acquired by randomly changing the placement and orientation of the rocks, following a similar procedure as that described in Chatterjee et al. (2010b). Fig. 5 shows sample color images of the five lithologies. It can be observed that many of the rocks have some overlap or are adjacent to neighboring rocks with no background between them. The database was divided into 10 subsets, and a leave-one-out cross validation was performed using 9 subsets for training and one for validation in performing the experiments. The same number of examples of each class was used in the training stage. The mean number of rock sub-images (more than 90% of rock, Section 2.4.1) in each image was 650. Therefore, the SVM was trained with approximately 23400 examples of each class and tested with approximately 2600 examples of each class in each iteration of the cross validation. In each experiment, the optimal parameters of the SVM were searched on a grid with a logarithmic scale using a 5-fold cross validation in a subset of the training set. The values of the grid were in the range $\log_2(C) = [-6, 15]$ and $\log_2(\gamma) = [-14, 6]$ for C and γ, respectively. First, the search was performed using a step of length 2. Then, a fine-tuning of parameters around the first optimal point was carried out using a step of length 0.4. To search C and γ, 1% of the available sub-images was randomly selected (approximately 234 examples of each class).

For testing each type of feature using the available information, the performance was first measured using color and range images together (see Table 1). Then, the two Gabor features with performances over 90% were used together with the best of the two tested LBP features. These features were tested using color and range images separately, and also using both images together (color + range in Table 2). The performance of the Gabor and LBP texture features in the color images transformed into grayscale, together with chromatic features to encode the color information, was also tested. The performance of the texture features computed in these gray images was tested using the gray images alone, and using gray and laser range images together (gray + range in Table 2). Additionally, the classification performance obtained using only chromatic features was computed.

Finally, a feature selection method based on mutual information (Estevez et al., 2009; Vergara and Estévez, 2014) was used to analyze the number of features required in the classification. We chose the CMIM feature selection method (Brown et al., 2012; Fleuret, 2004; Guyon et al., 2006; Wang and Lochovsky, 2004) because it selects relevant features, avoids redundancy, and includes variable complementarity. Also, unlike other methods that perform a transformation of the feature space, such as PCA, using CMIM makes it possible to select only the relevant features and to avoid the computation (or acquisition) of non-relevant features when the method is used for online classification. In each iteration of the feature selection method, CMIM selects the features that maximize the mutual information with the class to be predicted, given each one of the features already selected separately. CMIM considers that a feature is relevant only if it provides high information about the predicted class, and if this information is not contained in any of the features already selected (Tapia et al., 2016). A comparison between the result obtained by using CMIM and by using the classical PCA method was also carried out. In the comparison, the number of principal components selected was equal to the minimum number of features selected by CMIM with which the rock classification performance is not significantly affected. The classification method was implemented in Matlab for training and testing.

Table 1
Classification performance based on sub-images and rock boundaries, considering different types of features, and using the color + range images. The best performances achieved by the Gabor and LBP features are marked in bold. The SVM was employed for classification based on sub-images, and then the classification was improved by using voting among the sub-images within the rock boundary. The table shows the results obtained with a leave-one-out 10-fold cross validation. In each iteration of the cross validation, the SVM was trained and tested with approximately 23400 and 2600 sub-images of each class, respectively (see Section 3). The results are in the format [mean] ± [standard deviation].

	Sub-image classification		Rock classification	
Feature	Training set	Validation set	Training set	Validation set
G_M	81.55 ± 0.22	76.95 ± 2.14	96.75 ± 0.16	94.26 ± 2.40
G_{MP}	100.00 ± 0.00	88.25 ± 1.42	100.00 ± 0.00	98.88 ± 0.81
G_{stat}	93.31 ± 0.27	**90.01 ± 0.68**	99.30 ± 0.03	97.69 ± 0.84
G_{rea}	96.35 ± 0.09	**90.84 ± 0.68**	99.74 ± 0.09	97.66 ± 1.10
G_{DFT}	100.00 ± 0.00	84.23 ± 1.31	100.00 ± 0.00	98.41 ± 0.79
LBP^{riu2}	84.69 ± 0.09	81.40 ± 1.05	98.88 ± 0.08	97.85 ± 0.83
BRINT_CS_CM	93.24 ± 0.09	**86.50 ± 1.03**	99.86 ± 0.03	98.93 ± 0.57

4. Results

Table 1 shows the classification performance of the proposed method by sub-images and by rock boundary, using each of the Gabor and LBP texture features. The features were computed in the color + range images, and became the inputs to the SVM that was used for classification. The classification by sub-images assesses the performance of each type of feature. The classification by rock boundary is affected by the rock segmentation. Table 1 shows that the Gabor features with the best performance were G_{stat} and G_{rea} (marked in bold) which includes rotation invariance; and the LBP feature with the best performance was BRINT_CS_CM (marked in bold). Results in Table 1 shows that the performance of all the features, using color + range images, are significantly higher than the previous reported results in both, classification by sub-images

Fig. 5. Examples of the five different lithologies included in the database: (a) Andesite, (b) Dacitic Diatreme, (c) Rhyolitic Diatreme, (d) Porphyritic Dykes and (e) Other Breccias.

Table 2
Percentage of correct classification of sub-images based on combinations of the best features (shown in Table 1). The best performance is marked in bold. Tests were performed on the color image alone, the range image alone, color + range images, color images transformed into grayscale, and gray + range images. The chromatic features were used to encode the color information when gray images were used. The performance achieved using only the chromatic features is also shown. The results shown in Table 2 were obtained using a leave-one-out 10-fold cross validation method. In each iteration of the cross validation, the SVM was trained and tested with approximately 23400 and 2600 sub-images of each class, respectively (see Section 3). The results are in the format [mean] ± [standard deviation].

		Sub-image classification		Rock classification	
Features	Image Type	Training set	Validation set	Training set	Validation set
G_{stat} + BRINT_CS_CM	Color	100.00 ± 0.00	86.85 ± 0.98	100.00 ± 0.00	98.10 ± 0.67
G_{stat} + BRINT_CS_CM	Range	69.49 ± 0.11	64.52 ± 1.19	91.00 ± 0.18	88.35 ± 1.95
G_{stat} + BRINT_CS_CM	Color + range	95.92 ± 0.13	91.52 ± 0.35	99.86 ± 0.03	98.72 ± 1.10
G_{rea} + BRINT_CS_CM	Color	100.00 ± 0.00	87.52 ± 1.91	100.00 ± 0.00	97.77 ± 1.52
G_{rea} + BRINT_CS_CM	Range	75.02 ± 0.14	65.94 ± 1.75	94.45 ± 0.19	89.65 ± 2.50
G_{rea} + BRINT_CS_CM	Color + range	96.46 ± 0.11	**92.65 ± 1.45**	99.81 ± 0.07	**99.24 ± 0.87**
G_{stat} + BRINT_CS_CM + chroma	Gray	80.96 ± 0.11	70.29 ± 1.56	96.13 ± 0.15	89.67 ± 2.16
G_{stat} + BRINT_CS_CM + chroma	Gray + range	81.66 ± 0.09	78.66 ± 1.05	97.21 ± 0.14	96.04 ± 1.23
G_{rea} + BRINT_CS_CM + chroma	Gray	76.47 ± 0.18	69.94 ± 1.23	93.94 ± 0.13	89.18 ± 1.96
G_{rea} + BRINT_CS_CM + chroma	Gray + range	84.42 ± 0.12	79.21 ± 2.16	98.01 ± 0.20	96.45 ± 1.67
Chroma	Color	51.27 ± 0.19	50.14 ± 1.82	58.00 ± 0.53	58.64 ± 3.10

and by rock boundary. In order to verify the statistical significance ($p < 0.05$) of the differences between the sub-image classification performances, an analysis of variance (ANOVA), and a multiple comparison test were carried out. The Fisher's least significant difference procedure was used in the multiple comparison test. The performance of the feature with best performance, G_{rea}, has only a non-significant difference from the second best feature, G_{stat}. Feature G_{stat} has a non-significant difference from G_{rea} and G_{MP}. The best LBP feature, BRINT_CS_CM, has significant differences from all other features.

Table 2 shows the classification performance using combinations of the best features from Table 1. Table 2 also shows the performance of those features computed in the color images transformed into grayscale together with the chromatic features to encode the color information. The results were computed using a leave-one-out 10-fold cross validation. It can be inferred from the results that the best performances were obtained using color + range images, followed by the results obtained using only color, and only range images. The best performance was achieved by the combination of features G_{rea} and BRINT_CS_CM, computed in the color + range images (marked in bold in Table 2). This feature combination reached a performance of 92.65% accuracy with the sub-image classification, and 99.24% with the rock boundary classification. Our method classified 14.4% more sub-images correctly than was reported in the last publication of work with the same sets of rocks (Perez et al., 2015), that showed a performance of 84.8%. In order to verify that the sub-image classification performances are statistically different ($p < 0.05$), an ANOVA test was performed. Then, a multiple comparison test using the Fisher's least significant difference procedure was carried out. The performances of the two features with best performance, G_{rea} + BRINT_CS_CM and G_{stat} + BRINT_CS_CM, have non-significant differences between them, but they are statistically different from the other types of features.

Fig. 6 shows the classification performance of the best case considering combinations of features G_{rea} + BRINT_CS_CM in color + range images when the number of features is reduced using the CMIM method. The figure shows that even if only 10% of the features are used (144 features), a performance of over 99% is achieved in the rock classification, and of 88.56% in the sub-image classification. This result is very important because it allows a reduction in the number of computations by ignoring 90% of the extracted features, without significantly affecting classification performance. This reduction in the number of required features has a direct impact on the computational time required to operate a rock type classification system.

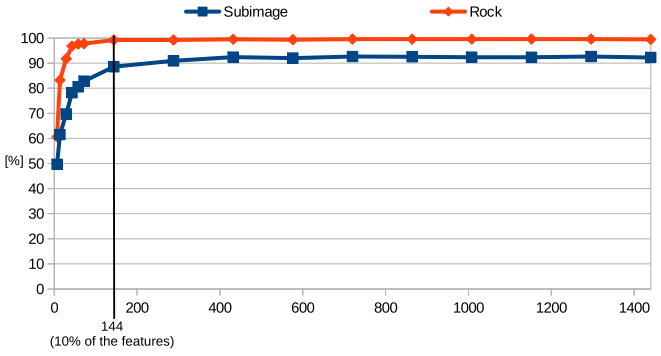

Fig. 6. Classification performance of the feature combination G_{rea} and BRINT_CS_CM as the number of features is reduced. The CMIM method was used to select the most relevant features. The features were computed in color + range images. The graph shows the results of the sub-image and rock classifications.

Fig. 7 shows the percentage of G_{rea} and BRINT_CS_CM features, computed in color or range images, selected as the number of features is reduced using the CMIM method. As can be observed in Fig. 7, the percentage of features computed in the range image does not decrease as the number of features is reduced. This indicates that the

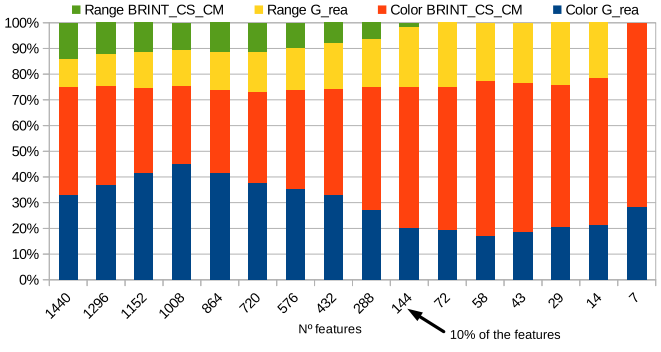

Fig. 7. Percentage of G_{rea} and BRINT_CS_CM features, computed in color or range images, selected when the number of features used is reduced using the CMIM method. The feature reduction was computed based on the best case obtained, which uses the combination of features G_{rea} + BRINT_CS_CM in color + range images. Fig. 6 shows the classification performance as the number of features is reduced.

3D texture features are relevant for rock classification. It can also be noted that the percentage of Gabor and LBP features stays relatively constant as the number of features decreases. This demonstrates that both types of features are relevant and complementary in rock type classification.

In order to perform a comparison between the result obtained by using CMIM and by using the classical PCA method, the first 144 principal components of the training features obtained using G_{rea} + BRINT_CS_CM were computed in each iteration of the cross validation. The first 144 principal components explain 79.57% of the total variance in the features. The performance in sub-image classification obtained by using PCA was $85.22 \pm 1.32\%$ (Fig. 6) and by using CMIM it was $88.58 \pm 1.55\%$. This difference is statistically significant with a p-value = 2.96e−05 using a two-sample t-test.

4.1. Comparison with our previous work

The same set of rock samples was used in this work as in our previous work Perez et al. (2015) making the results comparable.

In Perez et al. (2015), 40 images from each lithology were acquired using a digital IP-camera. The image size was 2048 × 1536 pixels. The images were tessellated into sub-images of 64 × 48 pixels, i.e., each axis was divided into 32 sections. The features were computed using Gabor filters with 8 orientations, and 5 spatial scales. The mean and standard deviation of the magnitude of the Gabor filters in each sub-image were used as features. The features were computed in each channel of the HSV color space, and then were concatenated in a feature vector. These features are equivalent to G_M in the current work. An SVM was used to classify the sub-images. A second classification was performed based on voting among sub-images that fall within the rock contour. Morphological operations and the watershed transform method were used to segment the rocks in the color images.

Table 3 shows a comparison between the results reported in Perez et al. (2015) and those of our present work. The feature G_M is the same type of feature as was used in Perez et al. (2015), and therefore it is included in Table 3. The feature G_{rea} + BRINT_CS_CM is also included since it is the feature with the best performance in the current work. Table 3 shows that the performance is improved if G_M is used in the new color images. This improvement is probably caused by the better resolution of the new images, 3072 columns compared with 2048. The classification performance is not improved if G_M is used in color + range images. Nevertheless, when the features G_{rea} + BRINT_CS_CM are used in color + range images, the performance improves. This shows that the feature G_M is not suitable for extracting information from the 3D texture.

5. Conclusions

Rock classification is an important task in mining operations. Classification information can be used to control many processes, such as grinding or mine planning. The aim of this study was to develop a new method of rock type classification using color and laser range images. According to our literature review, this is the first method that uses 3D laser range features from rocks to classify rock type. Our study shows that the 3D laser range features can be used to improve rock type classification significantly.

The images were tessellated into sub-images and a classification process with two stages was performed. In the first stage, every sub-image was classified using an SVM. In the second stage, a voting process was performed among the sub-images within the rock boundary to improve the classification. The contour information of each rock was used to select those sub-images intervening in the voting process. The experiments were performed using a database with 5 types of lithologies acquired from rocks on a conveyor belt for experimentation.

In order to use its complementary nature (Liao et al., 2009; Liu et al., 2014), different features based on Gabor filters, with and without rotation invariance, and LBP's were used in this study. Chromatic features were also tested with the aim of encoding the color information in these features, and the texture information in the Gabor and LBP's features.

A set of features was selected using a leave-one-out 10-fold cross validation in the database (Table 1). Then, combinations of these features were tested using different types of images (color, range, color + range, gray and gray + range) in an independent cross validation in the same database (Table 2). The classification performance obtained using only color images was better than that using only range images. Nevertheless, the best performance was obtained using color and range images together. This result shows that the 3D texture is useful for classifying rock type. The best performance was achieved by a combination of the features G_{rea} and BRINT_CS_CM. The feature G_{rea} is based on Gabor filters, and BRINT_CS_CM is based on LBP's (Liu et al., 2014). This result confirms the complementary nature of Gabor and LBP features. The results also show that the rotation invariance must be taken into account in rock type classification. Both features incorporate rotation invariance; G_{rea} rearranges the feature vector according to a main computed orientation, and BRINT_CS_CM takes the rotation invariance into account implicitly in its computation. The performance of the proposed classification method was very high, achieving the correct classification of 99.24% of the sub-images, which is higher than the best previously reported result with the same set of rocks which was 84.8% (Perez et al., 2015).

The CMIM feature selection method was used to analyze the number of features needed for classification. The result obtained, (99.22%) accuracy using only 10% of the features, was not significantly different from that obtained using all the features. This method allowed a reduction in the number of features from 1440 to 144 with no significant loss in classification performance. This set of 144 features still has some degree of redundancy; therefore, a greater reduction in the number of features could be achieved, but with a small drop in performance. For example, a classification performance of 96.8% was achieved using only 29 features (Fig. 6). Perhaps this performance could be improved by using another feature selection method in a future work. An important result is that the percentage of features computed in the range image is not reduced while the number of features is decreased. This result also shows that the 3D rock texture features are relevant in rock type classification.

Table 3
Comparison of the results of rock classification in our present work and those in Perez et al. (2015), which used the same set of rock samples. The results show the [mean] ± [standard deviation].

		Sub-image classification		Rock classification	
Features	Image type	Training set	Validation set	Training set	Validation set
G_M (Perez et al., 2015)	Color	70.50	66.90	86.80	84.80
G_M	Color	81.13 ± 0.37	76.46 ± 1.97	96.36 ± 0.24	93.48 ± 2.05
G_M	Color + range	81.55 ± 0.22	76.95 ± 2.14	96.75 ± 0.16	94.26 ± 2.40
G_{rea} + BRINT_CS_CM	Color + range	99.46 ± 0.11	92.65 ± 1.45	99.81 ± 0.07	99.24 ± 0.87

Acknowledgments

This work was supported by FONDECYT 3140574, FONDECYT 1161034, the Department of Electrical Engineering, and by the Advanced Mining Technology Center, Universidad de Chile. We want to thank Dr. Jorge R. Vergara for his implementation of the CMIM method.

References

Al-Batah, M.S., Isa, N.A.M., Zamli, K.Z., Sani, Z.M., Azizli, K.A., 2009. A novel aggregate classification technique using moment invariants and cascaded multilayered perceptron network. Int. J. Miner. Process. 92, 92–102. http://dx.doi.org/10.1016/j.minpro.2009.03.004.

Al-Thyabat, S., Miles, N.J., Koh, T.S., 2007. Estimation of the size distribution of particles moving on a conveyor belt. Miner. Eng. 20, 72–83. http://dx.doi.org/10.1016/j.mineng.2006.05.011.

Arivazhagan, S., Ganesan, L., Priyal, P., 2006. Texture classification using Gabor wavelets based rotation invariant features. Pattern Recogn. Lett. 27, 1976–1982. http://dx.doi.org/10.1016/j.patrec.2006.05.008.

Beucher, S., Lantuéjoul, C., 1979. Use of watersheds in contour detection. International Workshop on Image Processing: Real-time Edge and Motion Detection/Estimation, Rennes, France. pp. 17–21.

Bianconi, F., González, E., Fernández, A., Saetta, S.A., 2012. Automatic classification of granite tiles through colour and texture features. Expert Systems with Applications 39, 11212–11218. http://dx.doi.org/10.1016/j.eswa.2012.03.052.

Bieniek, A., Moga, A., 2000. An efficient watershed algorithm based on connected components. Pattern Recogn. 33, 907–916. http://dx.doi.org/10.1016/S0031-3203(99)00154-5.

Brown, G., Pocock, A., Zhao, M.J., Luján, M., 2012. Conditional likelihood maximisation: a unifying framework for information theoretic feature selection. J. Mach. Learn. Res. 13, 27–66.

Carlsson, O., Nyberg, L., 1983. A method for estimation of fragment size distribution with automatic image processing. First International Symposium on Rock Fragmentation by Blasting, Luleå, Sweden. pp. 333–345.

Casali, A., Gonzalez, G., Vallebuona, G., Perez, C., Vargas, R., 2001. Grindability soft-sensors based on lithological composition and on-line measurements. Miner. Eng. 14, 689–700.

Chang, C.C., Lin, C.J., 2011. LIBSVM: a library for support vector machines. ACM Trans. Intell. Syst. Technol. (TIST) 2, 27-27 http://dx.doi.org/10.1145/1961189.1961199.

Chatterjee, S., Bandopadhyay, S., Machuca, D., 2010a. Ore grade prediction using a genetic algorithm and clustering based ensemble neural network model. Math. Geosci. 42, 309–326. http://dx.doi.org/10.1007/s11004-010-9264-y.

Chatterjee, S., Bhattacherjeeb, A., Samanta, B., Pal, S.K., 2010b. Image-based quality monitoring system of limestone ore grades. Comput. Ind. 61, 391–408. http://dx.doi.org/10.1016/j.compind.2009.10.003.

Chaudhury, K.N., 2013. Acceleration of the shiftable o(1) algorithm for bilateral filtering and non-local means. IEEE Trans. Image Process. 22, 1291–1300. http://dx.doi.org/10.1109/TIP.2012.2222903.

Cortes, C., Vapnik, V., 1995. Support-vector networks. Mach. Learn. 20, 273–297. http://dx.doi.org/10.1023/A:1022627411411.

Estevez, P.A., Tesmer, M., Perez, C.A., Zurada, J.M., 2009. Normalized mutual information feature selection. IEEE Trans. Neural Netw. 20, 189–201. http://dx.doi.org/10.1109/TNN.2008.2005601.

Fernández, A., Ghita, O., González, E., Bianconi, F., Whelan, P.F., 2011. Evaluation of robustness against rotation of LBP, CCR and ILBP features in granite texture classification. Mach. Vis. Appl. 22, 913–926. http://dx.doi.org/10.1007/s00138-010-0253-4.

Fernández-Delgado, M., Cernadas, E., Barro, S., Amorim, D., 2014. Do we need hundreds of classifiers to solve real world classification problem? J. Mach. Learn. Res. 15, 3133–3181.

Fleuret, F., 2004. Fast binary feature selection with conditional mutual information. J. Mach. Learn. Res. 5, 1531–1555.

Gonçalves, L.B., Leta, F.R., S., de C.Valente, 2009. Macroscopic rock texture image classification using an hierarchical neuro-fuzzy system. 16th International Conference on Systems, Signals and Image Processing, 2009. IWSSIP 2009. http://dx.doi.org/10.1109/IWSSIP.2009.5367745.

Guo, Z., Zhang, L., Zhang, D., 2010. A completed modeling of local binary pattern operator for texture classification. IEEE Trans. Image Process. 19, 1657–1663. http://dx.doi.org/10.1109/TIP.2010.2044957.

Guyon, I., Gunn, S., Nikravesh, M., Zadeh, L.A. (Eds.), 2006. Feature extraction: foundations and applications (studies in fuzziness soft computing). Studies in Fuzziness and Soft Computing. Springer-Verlag, Berlin Heidelberg. http://dx.doi.org/10.1007/978-3-540-35488-8.

Guyot, O., Monredon, T., LaRosa, D., Broussaud, A., 2004. Visiorock, an integrated vision technology for advanced control of comminution circuits. Miner. Eng. 17, 1227–1235. http://dx.doi.org/10.1016/j.mineng.2004.05.017.

Han, J., Ma, K.K., 2007. Rotation-invariant and scale-invariant gabor features for texture image retrieval. Image Vis. Comput. 25, 1474–1481. http://dx.doi.org/10.1016/j.imavis.2006.12.015.

Hegenbart, S., Uhl, A., 2015. A scale- and orientation-adaptive extension of local binary patterns for texture classification. Pattern Recogn. 48, 2633–2644. http://dx.doi.org/10.1016/j.patcog.2015.02.024.

Isa, N.A.M., Sani, Z.M., Al-Batah, M.S., 2011. Automated intelligent real-time system for aggregate classification. Int. J. Miner. Process. 100, 41–50. http://dx.doi.org/10.1016/j.minpro.2011.04.009.

Kachanubal, T., Udomhunsakul, S., 2008. Rock textures classification based on textural and spectral features. International Journal of Computer, Electrical, Automation, Control and Information Engineering 2, 658–664.

Kim, H., Haas, C.T., Rauch, A.F., Browne, C., 2003. 3D image segmentation of aggregates from laser profiling. Comput. Aided Civ. Inf. Eng. 18, 254–263. http://dx.doi.org/10.1111/1467-8667.00315.

Koh, T.K., Miles, N.J., Morgan, S.P., Hayes-Gill, B.R., 2009. Improving particle size measurement using multi-flash imaging. Miner. Eng. 22, 537–543. http://dx.doi.org/10.1016/j.mineng.2008.12.005.

Lecun, Y., Bottou, L., Bengio, Y., Haffner, P., 1998. Gradient-based learning applied to document recognition. Proc. IEEE 86, 2278–2324. http://dx.doi.org/10.1109/5.726791.

Lee, J.R.J., Smith, M.L., Smith, L.N., Midha, P.S., 2005. A mathematical morphology approach to image based 3D particle shape analysis. Mach. Vis. Appl. 16, 282–288. http://dx.doi.org/10.1007/s00138-005-0181-x.

Lepistö, L., Kunttu, I., Autio, J., Visa, A., 2005. Rock image classification using color features in gabor space. J. Electron. Imaging 14, http://dx.doi.org/10.1117/1.2149872.

Liao, S., Law, M.W.K., Chung, A.C.S., 2009. Dominant local binary patterns for texture classification. IEEE Trans. Image Process. 18, 1107–1118. http://dx.doi.org/10.1109/TIP.2009.2015682.

Liu, L., Long, Y., Fieguth, P.W., Lao, S., Zhao, G., 2014. BRINT: binary rotation invariant and noise tolerant texture classification. IEEE Trans. Image Process. 23, 3071–3084. http://dx.doi.org/10.1109/TIP.2014.2325777.

Murtagh, F., Starck, J.L., 2008. Wavelet and curvelet moments for image classification: application to aggregate mixture grading. Pattern Recogn. Lett. 29, 1557–1564. http://dx.doi.org/10.1016/j.patrec.2008.03.008.

Oestreich, J.M., Tolley, W.K., Rice, D.A., 1995. The development of a color sensor system to measure mineral compositions. Miner. Eng. 8, 31–39. http://dx.doi.org/10.1016/0892-6875(94)00100-Q. minerals Engineering '94.

Ojala, T., Pietikäinen, M., Mäenpää, T., 2002. Multiresolution gray-scale and rotation invariant texture classification with local binary patterns. IEEE Trans. Pattern Anal. Mach. Intell. 24, 971–987. http://dx.doi.org/10.1109/TPAMI.2002.1017623.

Paclík, P., Verzakov, S., Duin, R.P.W., 2005. Improving the maximum-likelihood cooccurrence classifier: a study on classification of inhomogeneous rock images. In: Kalviainen, H., Parkkinen, J., Kaarna, A. (Eds.), Image Analysis. Lecture Notes in Computer Science vol. 3540. Springer Berlin Heidelberg., pp. 998–1008. http://dx.doi.org/10.1007/11499145_101.

Patel, A.K., Chatterjee, S., 2016. Computer vision-based limestone rock-type classification using probabilistic neural network. Geosci. Front. 7, 53–60. http://dx.doi.org/10.1016/j.gsf.2014.10.005.

Perez, C., Casali, A., Gonzalez, G., Vallebuona, G., Vargas, R., 1999. Lithological composition sensor based on digital image feature extraction, genetic selection of features and neural classification. 1999 International Conference on Information Intelligence and Systems. IEEE, Bethesda, Maryland, USA, pp. 236–241. http://dx.doi.org/10.1109/ICIIS.1999.810267.

Perez, C.A., Aravena, C.M., Vallejos, J.I., Estévez, P.A., Held, C.M., 2010. Face and iris localization using templates designed by particle swarm optimization. Pattern Recogn. Lett. 31, 857–868. http://dx.doi.org/10.1016/j.patrec.2009.12.029.

Perez, C.A., Estévez, P.A., Vera, P.A., Castillo, L.E., Aravena, C.M., Schulz, D.A., Medina, L.E., 2011. Ore grade estimation by feature selection and voting using boundary detection in digital image analysis. Int. J. Miner. Process. 101, 28–36. http://dx.doi.org/10.1016/j.minpro.2011.07.008.

Perez, C.A., Lazcano, V.A., Estévez, P.A., 2007. Real-time iris detection on coronal-axis-rotated faces. IEEE Trans. Syst. Man Cybern. Part C Appl. Rev. 37, 971–978. http://dx.doi.org/10.1109/TSMCC.2007.900647.

Perez, C.A., Saravia, J.A., Navarro, C.F., Schulz, D.A., Aravena, C.M., Galdames, F.J., 2015. Rock lithological classification using multi-scale gabor features from sub-images, and voting with rock contour information. Int. J. Miner. Process. 144, 56–64. http://dx.doi.org/10.1016/j.minpro.2015.09.015.

Pietikäinen, M., Ojala, T., Xu, Z., 2000. Rotation-invariant texture classification using feature distributions. Pattern Recogn. 33, 43–52. http://dx.doi.org/10.1016/S0031-3203(99)00032-1.

Potts, G., Ouchterlony, F., 2005. The capacity of image analysis to measure fragmentation: an evaluation using split desktop. Technical Report. Swedish Blasting Research Centre och Luleå tekniska universitet.,

Riaz, F., Hassan, A., Rehman, S., Qamar, U., 2013. Texture classification using rotation- and scale-invariant gabor texture features. IEEE Signal Process Lett. 20, 607–610. http://dx.doi.org/10.1109/LSP.2013.2259622.

Salinas, R.A., Raff, U., Farfan, C., 2005. Automated estimation of rock fragment distributions using computer vision and its application in mining. IEE Vision Image Signal Process. pp. 1–8. http://dx.doi.org/10.1049/ip-vis:20050810.

Singh, N., Singh, T.N., Tiwary, A., Sarkar, K.M., 2010. Textural identification of basaltic rock mass using image processing and neural network. Comput. Geosci. 14, 301–310. http://dx.doi.org/10.1007/s10596-009-9154-x.

Singh, V., Rao, S.M., 2006. Application of image processing in mineral industry: a case study of ferruginous manganese ores. Miner. Process. Ext. Metall. 115, 155–160. http://dx.doi.org/10.1179/174328506X109130.

Tapia, J.E., Perez, C.A., Bowyer, K.W., 2016. Gender classification from the same iris code used for recognition. IEEE Trans. Inf. Forensics Secur. 11, 1760–1770. http://dx.doi.org/10.1109/TIFS.2016.2550418.

Tessier, J., Duchesne, C., Bartolacci, G., 2007. A machine vision approach to on-line estimation of run-of-mine ore composition on conveyor belts. Miner. Eng. 20, 1129–1144. http://dx.doi.org/10.1016/j.mineng.2007.04.009.

Thurley, M.J., 2002. Three Dimensional Data Analysis for the Separation and Sizing of Rock Piles in Mining. Ph.D. thesis. Monash University.
Thurley, M.J., 2009. Fragmentation size measurement using 3D surface imaging. Ninth International Symposium on Rock Fragmentation by Blasting–FRAGBLAST, Granada, Spain. pp. 133–140.
Thurley, M.J., 2011. Automated online measurement of limestone particle size distributions using 3D range data. J. Process Control 21, 254–262. http://dx.doi.org/10.1016/j.jprocont.2010.11.011.
Thurley, M.J., Andersson, T., 2008. An industrial 3D vision system for size measurement of iron ore green pellets using morphological image segmentation. Miner. Eng. 21, 405–415. http://dx.doi.org/10.1016/j.mineng.2007.10.020.
Thurley, M.J., Ng, K.C., 2005. Identifying, visualizing, and comparing regions in irregularly spaced 3D surface data. Comput. Vis. Image Underst. 98, 239–270. http://dx.doi.org/10.1016/j.cviu.2003.12.002.
Thurley, M.J., Ng, K.C., 2008. Identification and sizing of the entirely visible rocks from a 3D surface data segmentation of laboratory rock piles. Comput. Vis. Image Underst. 111, 170–178. http://dx.doi.org/10.1016/j.cviu.2007.09.009.
Vergara, J.R., Estévez, P.A., 2014. A review of feature selection methods based on mutual information. Neural Comput. & Applic. 24, 175–186. http://dx.doi.org/10.1007/s00521-013-1368-0.
Wang, G., Lochovsky, F.H., 2004. Feature selection with conditional mutual information MaxiMin in text categorization. Thirteenth ACM International Conference on Information and Knowledge Management (CIKM), New York, USA. pp. 342–349. http://dx.doi.org/10.1145/1031171.1031241.
Wang, W., 2006. Image analysis of particles by modified ferret method – best-fit rectangle. Powder Technol. 165, 1–10. http://dx.doi.org/10.1016/j.powtec.2006.03.017.
Zhang, J., Tan, T., 2002. Brief review of invariant texture analysis methods. Pattern Recogn. 35, 735–747. http://dx.doi.org/10.1016/S0031-3203(01)00074-7.
Zhao, G., Ahonen, T., Matas, J., Pietikäinen, M., 2012. Rotation-invariant image and video description with local binary pattern features. IEEE Trans. Image Process. 21, 1465–1477. http://dx.doi.org/10.1109/TIP.2011.2175739.